Journal of the Physical Society of Japan **86**, 074706 (2017)
https://doi.org/10.7566/JPSJ.86.074706

Spin-1/2 Quantum Antiferromagnet on a Three-Dimensional Honeycomb Lattice Formed by a New Organic Biradical F_4BIPBNN

Naoki Amaya[1], Toshio Ono[1], Yuta Oku[1], Hironori Yamaguchi[1], Akira Matsuo[2], Koichi Kindo[2], Hiroyuki Nojiri[3], Fernando Palacio[4], Javier Campo[4], and Yuko Hosokoshi[1]*

[1]*Department of Physical Science, Osaka Prefecture University, Sakai 599-8531, Japan*
[2]*The Institute for Solid State Physics, The University of Tokyo, Kashiwa, Chiba 277-8581, Japan*
[3]*Institute for Materials Research, Tohoku University, Sendai 980-8577, Japan*
[4]*Department of Condensed Matter Physics, and Institute of Materials Science of Aragón, CSIC–University of Zaragoza, 50009 Zaragoza, Spain*

(Received May 4, 2017; accepted May 22, 2017; published online June 16, 2017)

We have succeeded in synthesizing a new organic biradical F_4BIPBNN [= 2,2′-(3,3′,5,5′-tetrafluorobiphenyl-4,4′-diyl)bis(4,4,5,5-tetramethylimidazolin-1-oxyl 3-oxide)] which forms an $S = 1/2$ Heisenberg three-dimensional honeycomb antiferromagnet. Each site of a honeycomb layer alternately couples with upper or lower layers, which results in the unique three-dimensional honeycomb network with four nearest neighbors. At zero magnetic field, antiferromagnetic long-range order has been observed below $T_N = 2.7$ K. Magnetic susceptibility in both paramagnetic and antiferromagnetic states and the magnetization curves are well reproduced by quantum Monte Carlo calculations with three antiferromagnetic interactions in the range of 4.3 to 6.6 K. From the concave shape of the magnetization curve, the shrinkage of spin due to spin fluctuations is evaluated to approximately 30% with respect to its classical value. The phase diagram of magnetic field versus temperature was determined by heat capacity and magnetization. In the field region below 3 T, a slight increase of T_N was observed, which reflects the effect of spin fluctuations.

1. Introduction

Purely organic magnets with π-electron spins have essentially negligible small spin–orbit couplings and are attractive materials because they are archetypical $S = 1/2$ Heisenberg spin systems in which quantum fluctuations play an important role. The antiferromagnetic frameworks of isotropic $S = 1/2$ spins connected by the small number of the nearest neighbors are the key factors of the novel magnetic states arising from quantum fluctuations. Among the representative stable organic radical skeletons, the nitroxide (–N–O•) radical has the advantage of making an antiferromagnetic spin network by the intermolecular contact between the NO groups.[1,2] The stacking of planar π-conjugated molecules gives a one-dimensional (1D) network. For a polyradical system in which two or more NO groups are substituted on a planar molecule, such as a benzene or a biphenyl, a double spin chain with different spin size has been reported.[2,3] Besides extensive studies on the 1D Heisenberg antiferromagnet, growing attention is being paid to the effect of quantum fluctuations in two- or three-dimensional (2D or 3D) Heisenberg antiferromagnets with the small number of the nearest neighbors (z), but the experimental realization is still rare.

An efficient strategy to realize high-dimensional spin networks is the molecular designing of twisted π-planes, each of which has multidirectional magnetic exchange pathways. There is an example in a biradical system that the molecular arrangement of an 1D stacking has been changed to a 2D honeycomb arrangement by the enlargement of the dihedral angle between the two radical planes.[1] In order to realize a 3D spin network, we have designed an organic biradical involving two nitronyl nitroxide (NN) units that are coupled through twisted π-planes. The NN unit consists of two conjugated NO groups and has exchange pathways in two directions. As discussed later in this paper, we have found that a new organic biradical F_4BIPBNN [= 2,2′-(3,3′,5,5′-tetrafluorobiphenyl-4,4′-diyl)bis(4,4,5,5-tetramethylimidazolin-1-oxyl 3-oxide)] forms a 3D honeycomb antiferromagnet with four magnetic exchange pathways at each site of $S = 1/2$. Each site of a honeycomb layer is alternately connected to upper or lower layers to realize alternate stacking of honeycomb layers.

There is rare example of 3D magnetic lattice in which the smallest number of the nearest neighbors is $z = 4$. The representative model without frustration is a diamond lattice that has three-fold stacking of honeycomb layers with $z = 4$. A diamond lattice with $S = 5/2$ was reported for a Mn compound with disordered structure.[4] For the case of $S = 1/2$ system, only $[\{Rh_2(acam)_4\}_2I]_n \cdot 6nH_2O$ has been reported as an distorted diamond lattice with the small Weiss constant of -4 K.[5]

In this paper, we have succeeded in synthesizing a new organic biradical F_4BIPBNN, which forms a new 3D honeycomb antiferromagnet with $z = 4$. The crystal structure and magnetic properties have been examined. Two kinds of intermolecular interactions, together with the intramolecular interactions form a 3D honeycomb network of $S = 1/2$. The magnetic interactions have been evaluated by quantum Monte Carlo (QMC) calculations to be in the same order within the rage of 4.3–6.6 K. The 3D long range order was observed at $T_N = 2.7$ K, which is well reproduced by the 3D honeycomb model. The concave shaped magnetization curve was observed and the shrinkage of spin due to the effect of quantum fluctuations is evaluated to approximately 30% with respect to its classical value. The effect of quantum fluctuations also appears in the slight increase of T_N with the increase of magnetic field. This study is the first observation of the effect of quantum fluctuations among 3D lattice, caused by the unique network of ideally isotropic spins of $S = 1/2$ coupled with the minimum exchange pathways of $z = 4$.

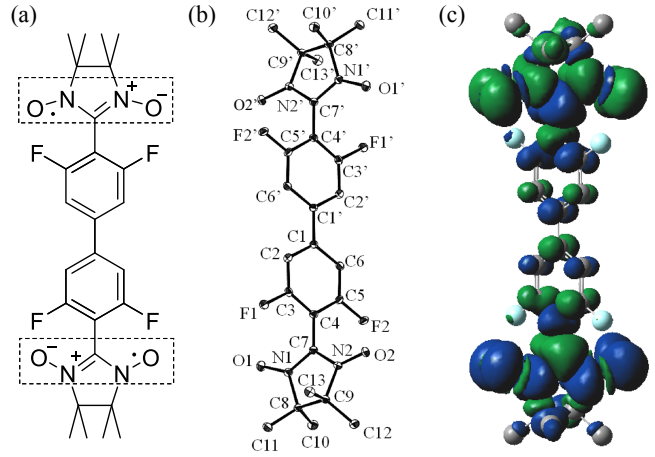

Fig. 1. (Color online) (a) Molecular structure of F_4BIPBNN. The nitronyl nitroxide (NN) unit is marked by a dashed rectangle. (b) ORTEP view of a molecule determined at 23 K with atomic labelling. Ellipsoids are scaled to enclose 50% of the electronic density. Hydrogen atoms are omitted. (c) Spin density distribution of F_4BIPBNN determined by MO calculation for the crystallographic coordinates at 23 K. Blue and green lobes represent positive and negative spin densities, respectively.

Table I. Crystallographic data of F_4BIPBNN.

	Temperature/K	
	293(2)	23(2)
Formula	$C_{26}H_{28}F_4N_4O_4$	
Crystal system	Monoclinic	
Space group	$P2_1/n$	
Z	2	
Radiation	Mo Kα ($\lambda = 0.71070$ Å)	
a/Å	10.766(2)	10.660(2)
b/Å	10.4126(18)	10.3537(18)
c/Å	12.380(3)	12.079(2)
β/°	114.447(4)	113.411(4)
V/Å^3	1263.4(4)	1223.7(4)
D_{calc}/g cm^{-3}	1.411	1.457
Total reflections	2612	2618
Reflection used ($I > 2\sigma(I)$)	1865	2383
Parameters refined	176	228
Residuals: R; R_w	0.0374; 0.0953	0.0373; 0.0886
Goodness of fit	1.000	1.041

2. Experimental Procedure

The synthesis of F_4BIPBNN, whose molecular structure is shown in Fig. 1(a), was carried out following the conventional procedure[6,7] starting from 1-bromo-3,5-difluorobenzene through four steps. The obtained compounds were purified by column chromatography on silica gel with chloroform and ethyl acetate. Recrystallization of slow evaporation from a concentrated acetonitrile solution in heptane atmosphere at 70 °C yielded purple plate single crystals of F_4BIPBNN.

X-ray diffraction data were collected on a Rigaku AFC-8R Mercury CCD RA-Micro7 diffractometer with a Japan Thermal Engineering XR-HR10K at the temperatures of 293 and 23 K. The crystal structure was solved by direct methods and refined by the full-matrix least-squares technique using SHELX-97 software.[8] The structural refinement was carried out using anisotropic and isotropic thermal parameters for the nonhydrogen atoms and the hydrogen atoms, respectively.

Magnetic measurements of non-oriented single crystals were obtained on a Quantum Design MPMS XL SQUID magnetometer at magnetic fields spanning from 0.05 to 5 T over the temperature range of 1.8–300 K. Furthermore, the VSM option on a Quantum Design Physical Properties Measurement System (PPMS) was employed to measure the temperature dependence of magnetization in various magnetic fields below 10 K over the field range of 5–9 T at a temperature upsweep of 3 K/min. The experimental susceptibility was corrected for theoretical diamagnetic contributions using Pascal's constants to give the molar paramagnetic susceptibility. Magnetization curves up to 23 T, at low temperatures ($T = 0.4$, 1.7, and 4.2 K) were obtained by an inductive method in pulsed magnetic fields at IMR, Tohoku University.[9] A pulsed magnetic field with nearly sinusoidal shape was generated with the rise time of 6 msec. Magnetization curves were normalized by the saturation value.

The specific heats of several single crystals of F_4BIPBNN were measured by a thermal relaxation method using the Quantum Design PPMS installed at Osaka Prefecture University and ISSP, University of Tokyo. The measurements at zero and in the magnetic field up to 7 T were done in the temperature range of 1.9–100 K. For the measurements in the range of $T = 0.5$–7 K and $B = 9$–14 T, measurements were performed with the Helium-3 refrigerator installed at ISSP, University of Tokyo.

The ab initio molecular orbital (MO) calculations were performed using the software package Gaussian09. The UB3LYP method was applied as broken symmetry (BS) hybrid density functional theory (DFT) calculations with the basis set 6-31G. The calculations were carried out on real molecules employing our crystallographic atomic coordinates at 293 and 23 K. The convergence criterion was 10^{-7} hartree. The magnetic exchange interaction between neighboring radical units were estimated based on the formula proposed by Yamaguchi.[10]

QMC simulations were performed with the loop[11,12] and dirloop_sse[12,13] packages involved in the ALPS project to obtain, respectively, the magnetic zero-field susceptibility versus temperature and the magnetization versus magnetic field curves. The calculations were performed for different system sizes ($N = 512, 1000, 1728$) under periodic boundary condition for $S = 1/2$ spin.

3. Results

3.1 Crystal structure

The crystallographic information measured at 293 and 23 K is summarized in Table I. Since the space group and the relative relation of the lattice constants did not change for either temperature, we concluded that there is no structural change down to 23 K. An ORTEP drawing of a F_4BIPBNN molecule determined at 23 K is depicted in Fig. 1(b). The asymmetric unit is composed only of one half of the F_4BIPBNN molecule, owing to inversion symmetry. The dihedral angle between the best fit planes of O1–N1–C7–N2–O2, which is called nitronyl nitroxide (NN), and difluorobenzene has been determined as 62.7 and 61.4° at 293 and 23 K, respectively. The electrostatic repulsion between oxygen and fluorine atoms would be responsible for this large

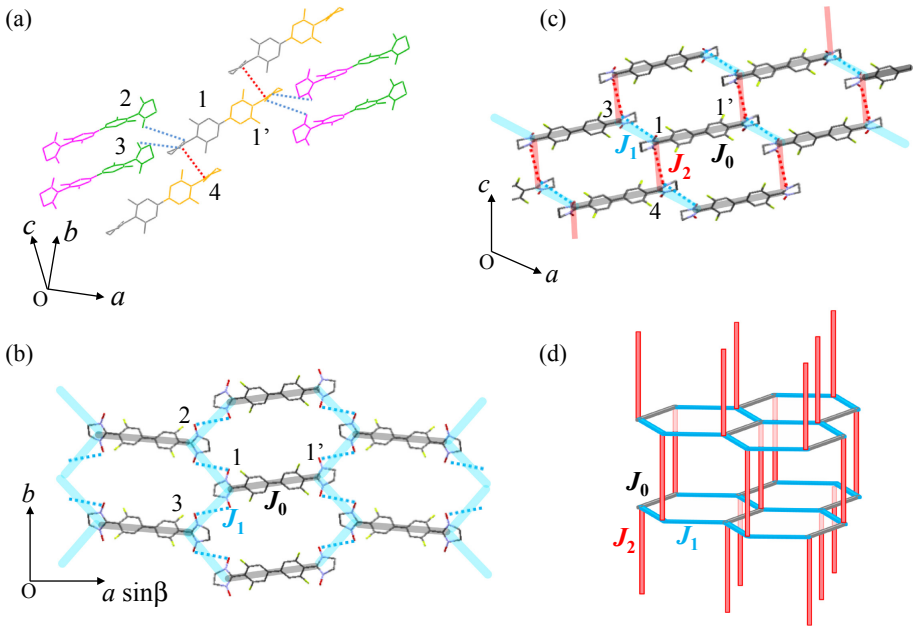

Fig. 2. (Color online) (a) Molecular packing at 23 K connected by NN short contacts within 5 Å. Blue and red dotted lines represent the interatomic contact of N–O 4.87 and 4.85 Å, respectively. Each asymmetric unit is colored by symmetry operation as grey (identity), yellow (inversion), green (two-fold screw), and pink (c-glide). Asymmetric unit (1) is surrounded by four neighbors with the notation of 1 (x, y, z), 1′ $(2-x, 2-y, 1-z)$, 2 $(1/2-x, 1/2+y, 1/2-z)$, 3 $(1/2-x, -1/2+y, 1/2-z)$, 4 $(1-x, 2-y, -z)$. All the definition is commonly used in (a), (b), and (c). (b) Molecular packing viewed along the c-axis. Each asymmetric unit carries an $S = 1/2$ spin, and the intramolecular interaction between (1) and (1′) is defined as J_0, and represented by grey thick line. The blue thick line represents the intermolecular interaction J_1 which connects (1) with (2) and (3). As a result, a honeycomb network of $S = 1/2$ consisting of J_0 and J_1 is formed. (c) Molecular packing viewed along the b-axis. The red thick line represents the intermolecular interaction J_2 which connects (1) with (4). In the ac-plane, a honeycomb network of $S = 1/2$ consisting of J_0, J_1, and J_2 is formed. (d) Magnetic model of F_4BIPBNN forming a 3D honeycomb lattice of $S = 1/2$ with four nearest neighbors, where grey, blue, and red bonds represent the intramolecular interaction J_0 and intermolecular interactions J_1 and J_2, respectively, between spins of $S = 1/2$ existing on each corner.

value. The spin density distribution determined by the MO calculation of the molecule is shown in Fig. 1(c). On each asymmetric unit that possesses a spin of $S = 1/2$, 88.8% of the total spin density is concentrated on the NN unit and only 7.2% is distributed on the difluorobenzene ring. Thus, a molecule is treated as two spins of $S = 1/2$ coupled through an intramolecular interaction J_0. Moreover, the intermolecular contacts between the NN units must be taken into account when we consider intermolecular interactions. In order to clarify the intermolecular packing, each methyl group (C10–C13) is omitted in Figs. 2(a)–2(c). There are two kinds of intermolecular contacts between the NN units within 5 Å, which are marked by blue and red dotted lines in Fig. 2(a). The blue line represents the interatomic contact of O1–N2, 4.97 Å at 293 K and 4.87 Å at 23 K between the molecules related by two-fold screw symmetry along the b-axis. The red line is the one between the molecules related by inversion symmetry with O2–N2, 4.90 Å at 293 K and 4.85 Å at 23 K, which connect molecules along the $a + c$ direction. The intermolecular interactions J_1 and J_2 are assigned to these intermolecular contacts between the NN units along the b-axis and the $a + c$ direction, respectively. As a result, each half of the molecule carrying an $S = 1/2$, is surrounded by four neighboring ones, as shown in Fig. 2(a). The half molecular unit (1) is connected with (1′) through the intramolecular interaction J_0, with (2) and (3) along the b-axis by the intermolecular interaction J_1, and with (4) by the intermolecular interaction J_2. The molecular packing viewed along the c- and b-axis are shown in Figs. 2(b) and 2(c), respectively, where a honeycomb network of $S = 1/2$ is formed in each of the a^*b- and ac-plane, where a^* is defined as $a \sin \beta$. In the a^*b-plane, a 1D chain with J_1 is connected by J_0 to form a honeycomb network as shown in Fig. 2(b). Each hexagonal unit with J_0–J_1–J_1–J_0–J_1–J_1 arrangement has chair conformation because the molecular long axis leans from the a^*b-plane by approximately 12°. We recall that F_4BIPBNN is a highly-twisted molecule. Thus, each corner of the J_0–J_1–J_1–J_0–J_1–J_1 honeycomb ring is alternately connected by J_2 with the upper and lower layers along the c-axis, as is shown in Fig. 2(c). As a result, the honeycomb network is spread in the ac-plane consisting of a hexagonal unit with J_0–J_1–J_2–J_0–J_1–J_2 arrangement. A schematic illustration of the magnetic model of this compound is drawn in Fig. 2(d). Grey, blue, and red bonds represent the magnetic interactions J_0, J_1, and J_2, respectively, between the spins of $S = 1/2$ on each corner. In this model, J_0 and J_2 are interchangeable, and a honeycomb network consisting of a hexagonal unit of J_2–J_1–J_1–J_2–J_1–J_1 arrangement is formed in the bc-plane. Therefore, the present compound forms the 3D network of $S = 1/2$ that comprises honeycomb layers in every three direction. Since each corner of a honeycomb layer is linked alternately to the upper or lower layer, honeycomb layers are linked in honeycomb fashion and each spin of $S = 1/2$ is magnetically coupled with $z = 4$.

Although a diamond lattice has common features with the present model that each site has $z = 4$ and honeycomb layers are seen in every three-direction, the difference lies in the stacking periodicity of the honeycomb layers. A diamond lattice has three-fold periodicity in the stack of honeycomb layers, where a honeycomb ring is not superimposed between

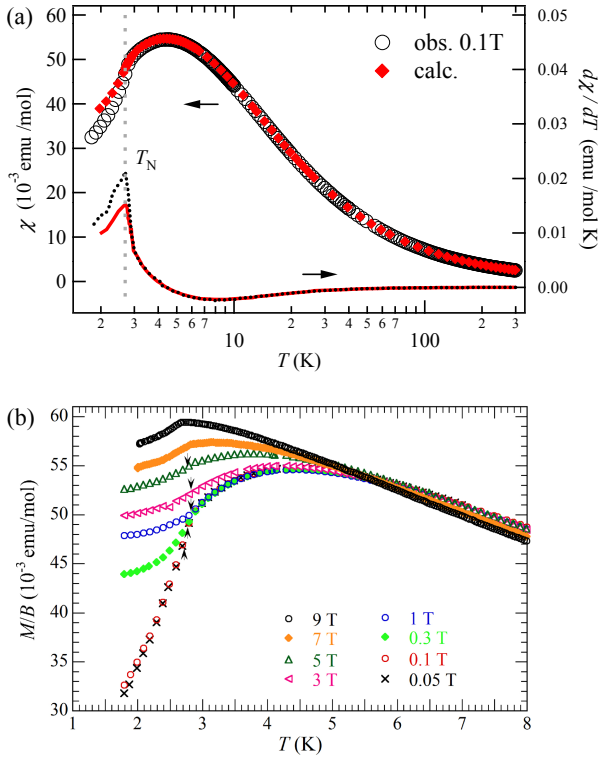

Fig. 3. (Color online) (a) Temperature dependence of magnetic susceptibility χ (= M/B) of F_4BIPBNN at $B = 0.1$ T (black circle) and the result of QMC calculation (red diamond) for a 3D honeycomb model with the parameter set of $J_0/k_B = 6.6$ K, $J_1/k_B = 4.3(2)$ K, $J_2/k_B = 5.9(3)$ K. Right axis shows the temperature dependence of the derivative of the susceptibility $d\chi(T)/dT$ at $B = 0.1$ T (black dotted line) and QMC calculation (red solid line). Dashed line on the T_N is a guide for eyes. (b) Temperature dependence of M/B for different magnetic fields at $B = 0.05$ T (cross), 0.1 T (red circle), 0.3 T (green diamond), 1 T (blue circle), 3 T (pink triangle), 5 T (green triangle), 7 T (orange diamond), and 9 T (grey circle). Arrow indicates T_N.

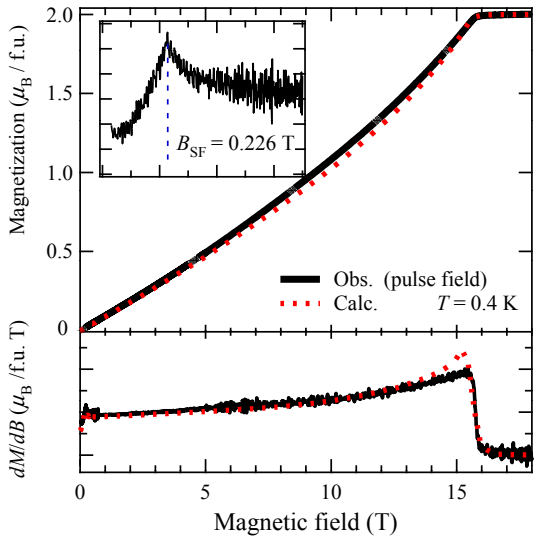

Fig. 4. (Color online) Magnetization curve at $T = 0.4$ K and its field derivative versus magnetic field (black solid line) for pulsed fields up to $B = 17$ T and theoretical curve (red dotted line) calculated with the same set of parameters [$J_0/k_B = 6.6$ K, $J_1/k_B = 4.3(2)$ K, $J_2/k_B = 5.9(3)$ K] as the susceptibility versus temperature curve. Inset: low magnetic field detail of the field derivative of the magnetization at 0.4 K. Spin flop (B_{SF}) and saturation (B_{SAT}) fields are 0.226 and 15.7 T, respectively.

the neighboring layers. On the other hand, the present model has two-fold periodicity in the stacking of honeycomb layers. When every corner is linked between superimposed honeycomb layers to both of the upper and lower layers, the model become a stacking honeycomb lattice with $z = 5$ whose honeycomb layers spread only in one direction. In the present case, the chair conformation of each honeycomb ring is the key of the interlayer contact at every other corner, which results in the honeycomb network in three direction. We call this unique 3D network with $z = 4$ here as a 3D honeycomb lattice in distinction from a diamond lattice.

3.2 Magnetic susceptibility

Figure 3(a) shows the continuous susceptibility versus temperature, $\chi(T) = M(T)/B$, measured in $B = 0.1$ T. Over the temperature range of 200–300 K, the Curie–Weiss law is followed with a Curie constant $C = 0.749(1)$ emu K/mol and a Weiss constant $\theta w = -16.2(1)$ K. The experimental Curie constant shows good agreement with the expected value of 0.753 emu K/mol, corresponding to 2 mol of spin $S = 1/2$ with $g = 2.0068$ reported for NN.[7] The negative value of the estimated Weiss constant indicates the existence of antiferromagnetic interactions.

The plot of χ vs T reveals a broad maximum at 4 K, which is a fingerprint of the development of short-range magnetic correlations, followed by a kink anomaly at 2.7 K, which suggests the occurrence of antiferromagnetic long-range order (AFM-LRO). The position of the kink is precisely determined to be 2.7 K by taking the temperature derivative of the susceptibility, $d\chi(T)/dT$, and we assigned it to be the Neel temperature, T_N. This was confirmed by heat capacity as described in Sect. 3.4.

Figure 3(b) displays a plot of M/B vs T measured in various magnetic fields up to 9 T. We noticed that there is a large change between 0.1 and 0.3 T, which implies the presence of the spin-flop transition between 0.1 and 0.3 T. It was also confirmed by the field dependence of the magnetization measured at low temperature, as described in the next subsection. The transition temperatures determined by the kink of the temperature dependence of the magnetization are indicated by the arrows in Fig. 3(b). The transition temperature T_N slightly increases with increasing applied magnetic field up to 3 T. Above 3 T, T_N shift toward lower-temperature side. The broad maxima of $\chi(T)$ continuously decrease with increasing magnetic fields, and at 9 T, it almost vanishes and the phase transition to the 3D AFM-LRO state is observed as a cusp-like extreme.

3.3 High-field magnetization curve

The high-field magnetization curve $M(B)$ measured at 0.4 K in pulsed magnetic fields up to 23 T is shown in Fig. 4 as a solid black line. The curve shows a saturation value of $2\mu_B$ per molecule at a field of 15.7 T. Two anomalies at magnetic fields $B_{SF} = 0.226$ T and $B_{SAT} = 15.7$ T are observed in the $dM(B)/dB$ curve at 0.4 K. The field dependence of the magnetization shows a concave curve and deviates from the classical linear behavior. This nonlinear behavior of magnetization versus magnetic fields comes from the shrinkage of spin due to the quantum mechanical zero-point oscillation of the spin. Since dM/dB at $B = 0$ is proportional to the magnitude of the spin at zero field $S_{B=0}$, we can evaluate the shrinkage factor of spin η,

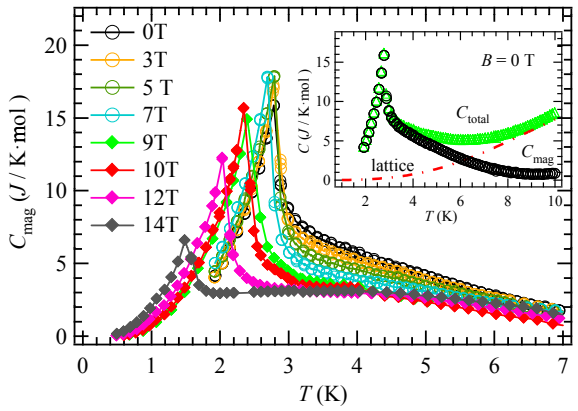

Fig. 5. (Color online) Temperature dependence of magnetic specific heat of F_4BIPBNN at zero magnetic field (black circle) and various magnetic fields $B = 3$ T (orange circle), 5 T (green circle), 7 T (blue circle), 9 T (green diamond), 10 T (red diamond), 12 T (pink diamond), and 14 T (grey diamond). Inset: Temperature dependence of specific heat of F_4BIPBNN at zero magnetic field. Magnetic specific heat C_{mag} (black circle) was obtained by subtracting lattice contribution (red dotted broken curve) from total specific heat C_{total} (green circle).

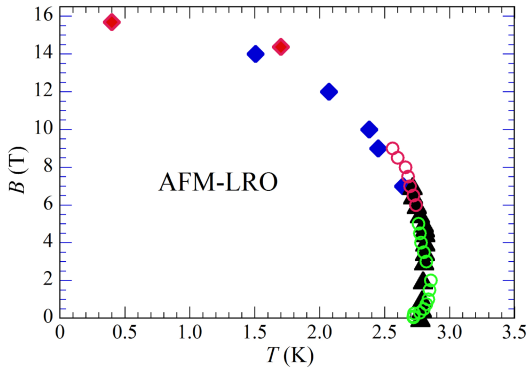

Fig. 6. (Color online) B–T phase diagram of F_4BIPBNN. Green and red circles represent T_N determined by susceptibility in separate measurements. Black triangles and blue diamonds present T_N determined by specific heat in separate measurements. Red diamonds indicate the saturation magnetization field observed in magnetization curves.

which is defined as $\eta = 1 - S_{B=0}/S$, by comparing with dM/dB of the classical spin system.[14] In the present system, the shrinkage factor of spin is evaluated as $\eta = 0.28$. This value has an intermediate magnitude between those of a 2D square lattice ($\eta = 0.39$)[15,16] and 3D cubic lattice ($\eta = 0.16$).[15,16] This result demonstrates that the magnetic properties of the present system exhibit the intermediate behavior between 2D and 3D systems.

3.4 Specific heat

The heat capacity versus temperature for different magnetic fields from 0 to 14 T is shown in Fig. 5. After subtraction from the total specific heat (C_{total}) of the lattice contribution ($C_{lattice}$), using a single Debye function with $\theta_D = 55$ K, the magnetic heat capacity (C_{mag}) was obtained (see the inset). A typical λ-shaped peak was observed at $T_N = 2.7$ K for $B = 0$. The total magnetic entropy gain (ΔS) was calculated by integrating C_{mag}/T with respect to T, where the low-temperature part of C_{mag} was extrapolated from observed data using the result of the spin-wave theory. The estimated value of ΔS at 7 K reaches 80% of $2N_A k_B \ln 2$, which is almost full entropy of two spins of $S = 1/2$ per molecule and the evidence of the 3D nature without frustration. When magnetic field increases up to 3 T, T_N slightly increases. With further increases of the magnetic field above 3 T, T_N shifts toward the lower-temperature side and the height of the peak decreases. The broad anomaly of short range correlation observed at approximately 4 K is depressed by increasing magnetic field. The magnetic field determined of T_N from the specific heat and the susceptibility gives the B–T phase diagram shown in Fig. 6.

4. Analysis and Discussion

4.1 Expectation of magnetic interactions by MO calculations

The present compound F_4BIPBNN, bearing two spins of $S = 1/2$, forms a 3D honeycomb lattice, where each $S = 1/2$ spin interacts with four neighboring spins with one J_0, two J_1 and one J_2 bonds. The former two forms the honeycomb network in the a^*b-plane and the last one connects the honeycomb layers in three-dimension. As described below, all three interactions should be antiferromagnetic according to the MO theory. Concerning the intramolecular interaction J_0,[17] the antiparallel spin alignment is stabilized by the spin polarization of the alternately appearing positive and negative spin density on π-conjugation, as shown in Fig. 1(c). The large spin density distribution on the NN unit comes from the fact that the singly occupied molecular orbital (SOMO) distributes on the NN unit. Since significant overlap between SOMOs always yields antiferromagnetic interaction,[1,2] the intermolecular interactions J_1 and J_2 are predicted to be antiferromagnetic.

The magnitude of the magnetic interaction is roughly estimated by applying Yamaguchi's formula[10] to the results of the MO calculation for the neighboring two asymmetric units connected by J_0, J_1, or J_2. The estimated values are $J_0/k_B = 13$ K, $J_1/k_B = 2.4$ K, and $J_2/k_B = 8.1$ K for the crystal structure at 293 K, and $J_0/k_B = 16$ K, $J_1/k_B = 2.7$ K, and $J_2/k_B = 8.9$ K for 23 K. The slight enhancement comes from the shrink of the crystallographic lattice with decreasing temperature. This procedure is the most commonly used but always gives overestimation of intramolecular interaction by a few times.[18,19] It comes from the spin contamination due to the fact that the pure singlet state is not described in the unrestricted MO theory. Assumption of the overestimation factor 0.380[19] predicts the intramolecular interaction $J_0/k_B \approx 6$ K. On the other hand, the planar analogue of F_4BIPBNN is reported to have the intramolecular interaction of 28 K.[20] When the reduction of the intramolecular interaction in a twisted molecule[1] is treated on the basis of the planarity factor $\cos\varphi_1 \cos\varphi_2$,[21] where φ denotes the dihedral angle between the radical unit and its connecting π-planes, F_4BIPBNN is expects to have $J_0/k_B \approx 6.5$ K. As for the intermolecular interactions, the order of the estimated values from MO calculations are always reliable.[22] The estimated values of J_1 and J_2 are consistent with the ones of related materials[1,2] when comparing the molecular packings. On assumption of the scaling factor for J_0, the magnitude of three interactions J_0, J_1, and J_2 are expected to be the same order at about 6 K. Although MO calculations are useful to reveal the intermolecular packing responsible for magnetic interactions, in order to determine the exact values of the

interactions, the analysis of the magnetic properties is essential.

4.2 *Analysis by QMC calculations and determination of magnetic interactions*

The determination of the magnetic interactions of the present compound has been done by the fitting of the magnetic susceptibility and of the magnetization curve with QMC calculations. We analyzed the magnetic susceptibility in terms of the 3D honeycomb lattice shown in Fig. 2(d). We assume the $S = 1/2$ Heisenberg spin Hamiltonian, which is expressed as

$$H = J_0 \sum_{\langle i,j \rangle} S_i \cdot S_j + J_1 \sum_{\langle k,l \rangle} (S_k \cdot S_l + S_k \cdot S_{l+1}) + J_2 \sum_{\langle m,n \rangle} S_m \cdot S_n, \quad (1)$$

where J_p $(p = 0, 1, 2)$ has positive value that indicates antiferromagnetic interactions, and the sums $\langle i,j \rangle$, $\langle k,l \rangle$, and $\langle m,n \rangle$ are taken for grey, blue and red bonds on Fig. 2(d), respectively. We calculated the magnetic susceptibilities by the QMC method for various combinations of the parameters of J_1/J_0 and J_2/J_0. The total value of the magnetic interactions $(J_0 + 2J_1 + J_2)$ is given by the saturation magnetic field $B_{SAT} = 15.7$ T. The agreement between the experiment and calculation was evaluated by using the quality function $(F)^2$ for each set of $(J_1/J_0, J_2/J_0)$,

$$(F(J_1/J_0, J_2/J_0))^2 = \sum_i (\chi_{calc}(T_i) - \chi_{obs}(T_i))^2. \quad (2)$$

The $(F)^2$ function was minimal for the set $J_0/k_B = 6.6$ K, $J_1/k_B = 4.3(2)$ K, $J_2/k_B = 5.9(3)$ K. The calculated results of $\chi(T)$ and $M(B)$ are compared with the experiments in Figs. 3(a) and 4, respectively. Since J_0 and J_2 are interchangeable in this magnetic model of Fig. 2(d), it is difficult to elucidate the intramolecular interactions J_0 as 6.6 K or 5.9 K. The alternative model with the intramolecular interaction $J_0/k_B = 5.9$ K, and intermolecular interactions $J_1/k_B = 4.3$ K and $J_2/k_B = 6.6$ K gives the identical calculated results. The estimated three kinds of antiferromagnetic interactions are in the range of 4.3 to 6.6 K, which are consistent with the expectation from the MO calculations.

4.3 *Quantum fluctuation in 3D honeycomb lattice*

Since the present 3D honeycomb lattice is the network of the ideally isotropic spins of $S = 1/2$ with $z = 4$, one can see some effect of quantum fluctuations, though it shows the AFM-LRO. The first evidence is the increase of T_N in low field regime as shown in Fig. 6. Similar behaviors have been often observed in quasi-1D Heisenberg antiferromagnets and have interpreted on the basis of the suppression of the quantum fluctuations by applying magnetic fields. Namely, T_N increases when the uniform moment is increased at the sake of the reduction of quantum shrinkage of spin in magnetic fields. In 2D Heisenberg antiferromagnets, the increase of T_N occurs when application of magnetic fields reduces the spin dimensionality and suppresses the quantum fluctuations along the field direction. This behavior is theoretically predicted[23,24] for the 2D square lattice Heisenberg antiferromagnet and observed in some model compounds.[25–27] In the present system, the magnetic interactions are not completely uniform and the three-dimensionality affords the gapless ground state. The observed field dependence of T_N indicates that the quantum fluctuations in this 3D system are suppressed by applying magnetic fields.

The effect of quantum fluctuations also appears in the non-linear magnetization curve shown in Fig. 4. From this concave shaped magnetization curve, the reduction of the magnetic moment due to the quantum fluctuations has been evaluated to $\eta = 0.28$, as described in Sect. 3.3. The effect of quantum fluctuations strikingly appears in $S = 1/2$ Heisenberg antiferromagnets, which is enhanced depending on the smaller value of z. Among them, the most conspicuous fluctuation of $\eta = 0.59$ is predicted[28] and observed[14] in the 1D chain lattice with $z = 2$. In higher dimensional system, spin fluctuations are still observed as $\eta = 0.39$[15,16] for the 2D square lattice with $z = 4$ and as $\eta = 0.16$[15,16] for the 3D cubic lattice with $z = 6$. It is evident that the spin fluctuations are more weakened in the 3D lattice which exhibits AFM-LRO. On the other hand, the present system shows significant spin fluctuations of $\eta = 0.28$ among 3D system in spite of the occurrence of AFM-LRO. Since this system is free from the effect of the spin frustration, the smallest value of $z = 4$ among 3D system is concluded to the key of the pronounced effect of the quantum fluctuation. This is the first observation of the quantum fluctuations among 3D magnetic lattice without spin frustration.

5. Conclusions

A 3D honeycomb lattice antiferromagnet of ideally isotropic spins of $S = 1/2$ with $z = 4$ has been firstly realized by an organic biradical F_4BIPBNN. The magnetic properties are well understood by three kinds of antiferromagnetic interactions in the same order of 4.2–6.6 K. The concave shaped magnetization curve was observed and the quantum fluctuations was evaluated as approximately 30% spin shrinkage. The AFM-LRO was observed and the B–T phase diagram was determined from the specific heat and susceptibility. The increase of T_N with applying magnetic field was observed in the low-field region, which is the evidence of quantum fluctuations in this 3D system. The present system is the first realization of the 3D quantum spin system without spin frustration. The observed quantum fluctuations are caused by the ideally isotropic nature of spins of $S = 1/2$ couples with the minimum exchange pathways of $z = 4$. In order to reveal precise spin structure in magnetic fields, further study such as NMR and neutron scattering is desirable. We hope that the present results stimulate the study of novel quantum spin states in 3D system.

Acknowledgments Dr. A. Arauzo from General Services for Research of University of Zaragoza is acknowledged. JC and FP acknowledge grant number MAT2015-68200-C2-2-P. This work was partly supported by JSPS KAKENHI Grant Number JP15H03695 for YH. This work was performed in part under the Inter-University Cooperative Research Program of the Institute for Materials Research, Tohoku University, and in Institute for Molecular Science, supported by Nanotechnology Platform Program (Molecule and Material Synthesis) of the Ministry of Education, Culture, Sports, Science and Technology (MEXT), Japan.

*yhoso@p.s.osakafu-u.ac.jp

1) Y. Hosokoshi, Y. Nakazawa, K. Inoue, K. Takizawa, H. Nakano, M. Takahashi, and T. Goto, Phys. Rev. B **60**, 12924 (1999).

2) K. Katoh, Y. Hosokoshi, K. Inoue, and T. Goto, J. Phys. Soc. Jpn. **69**, 1008 (2000).
3) Y. Hosokoshi, K. Katoh, Y. Nakazawa, H. Nakano, and K. Inoue, J. Am. Chem. Soc. **123**, 7921 (2001).
4) C. M. Kareis, S. H. Lapidus, P. W. Stephens, and J. S. Miller, Inorg. Chem. **51**, 3046 (2012).
5) Y. Fuma, M. Ebihara, S. Kutsumizu, and T. Kawamura, J. Am. Chem. Soc. **126**, 12238 (2004).
6) E. F. Ullman, J. H. Osiecki, D. G. B. Boocock, and R. Darcy, J. Am. Chem. Soc. **94**, 7049 (1972).
7) Y. Hosokoshi, M. Tamura, M. Kinoshita, H. Sawa, R. Kato, Y. Fujiwara, and Y. Ueda, J. Mater. Chem. **4**, 1219 (1994).
8) G. M. Sheldrick, SHELX97, Program for Crystal Structure Determination (University of Göttingen, Göttingen, 1997).
9) H. Nojiri, K.-Y. Choi, and N. Kitamura, J. Magn. Magn. Mater. **310**, 1468 (2007).
10) K. Yamaguchi, H. Fukui, and T. Fueno, Chem. Lett. **15**, 625 (1986).
11) S. Todo and K. Kato, Phys. Rev. Lett. **87**, 047203 (2001).
12) A. F. Albuquerque, F. Alet, P. Corboz, P. Dayal, A. Feiguin, S. Fuchs, L. Gamper, E. Gull, S. Gürtler, A. Honecker, R. Igarashi, M. Korner, A. Kozhevnikov, A. Läuchli, S. R. Manmana, M. Matsumoto, I. P. McCulloch, F. Michel, R. M. Noack, G. Pawlowski, L. Pollet, T. Pruschke, U. Schollwöck, S. Todo, S. Trebst, M. Troyer, P. Werner, and S. Wessel, J. Magn. Magn. Mater. **310**, 1187 (2007).
13) B. Bauer, L. D. Carr, H. G. Evertz, A. Feiguin, J. Freire, S. Fuchs, L. Gamper, J. Gukelberger, E. Gull, S. Guertler, A. Hehn, R. Igarashi, S. V. Isakov, D. Koop, P. N. Ma, P. Mates, H. Matsuo, O. Parcollet, G. Pawłowski, J. D. Picon, L. Pollet, E. Santos, V. W. Scarola, U. Schollwöck, C. Silva, B. Surer, S. Todo, S. Trebst, M. Troyer, M. L. Wall, P. Werner, and S. Wessel, J. Stat. Mech.: Theor. Exp. **2011**, P05001 (2011).
14) H. Mollymoto, E. Fujiwara, M. Motokawa, and M. Date, J. Phys. Soc. Jpn. **48**, 1771 (1980).
15) P. W. Anderson, Phys. Rev. **86**, 694 (1952).
16) R. Kubo, Phys. Rev. **87**, 568 (1952).
17) H. C. Longuet-Higgins, J. Chem. Phys. **18**, 265 (1950).
18) For example, K. Hayakawa, D. Shiomi, T. Ise, K. Sato, and T. Takui, J. Mater. Chem. **16**, 4146 (2006).
19) K. C. Ko, D. Cho, and J. Y. Lee, J. Phys. Chem. A **117**, 3561 (2013).
20) E. A. Mostovich, Y. Borozdina, V. Enkelmann, K. R. Langer, B. Wolf, M. Lang, and M. Baumgarten, Cryst. Growth Des. **12**, 54 (2012).
21) A. K. Pal, D. R. Mañeru, I. A. Latif, I. P. R. Moreira, F. Illas, and S. N. Datta, Theor. Chem. Acc. **133**, 1472 (2014).
22) H. Yamaguchi, S. Nagata, M. Tada, K. Iwase, T. Ono, S. Nishihara, Y. Hosokoshi, T. Shimokawa, H. Nakano, H. Nojiri, A. Matsuo, K. Kindo, and T. Kawakami, Phys. Rev. B **87**, 125120 (2013).
23) A. S. T. Pires, Phys. Rev. B **50**, 9592 (1994).
24) A. Cuccoli, T. Roscilde, R. Vaia, and P. Verrucchi, Phys. Rev. B **68**, 060402 (2003).
25) P. Sengupta, C. D. Batista, R. D. McDonald, S. Cox, J. Singleton, L. Huang, T. P. Papageorgiou, O. Ignatchik, T. Herrmannsdörfer, J. L. Manson, J. A. Schlueter, K. A. Funk, and J. Wosnitza, Phys. Rev. B **79**, 060409 (2009).
26) E. Čižmár, S. A. Zvyagin, R. Beyer, M. Uhlarz, M. Ozerov, Y. Skourski, J. L. Manson, J. A. Schlueter, and J. Wosnitza, Phys. Rev. B **81**, 064422 (2010).
27) Y. Kohama, M. Jaime, O. E. Ayala-Valenzuela, R. D. McDonald, E. D. Mun, J. F. Corbey, and J. L. Manson, Phys. Rev. B **84**, 184402 (2011).
28) R. B. Griffiths, Phys. Rev. **133**, A768 (1964).